Carbon 162 (2020) 528–544

Contents lists available at ScienceDirect

Carbon

journal homepage: www.elsevier.com/locate/carbon

Deconvoluting the XPS spectra for nitrogen-doped chars: An analysis from first principles

Michael Ayiania [a], Matthew Smith [a, b], Alyssa J.R. Hensley [b], Louis Scudiero [c], Jean-Sabin McEwen [a, b, d, e, f, **], Manuel Garcia-Perez [a, g, *]

[a] Department of Biological Systems Engineering, Washington State University, Pullman, WA, 99164, USA
[b] Gene and Linda Voiland School of Chemical Engineering and Bioengineering, Pullman, WA, 99164, USA
[c] Chemistry Department and Materials Science and Engineering Program, Pullman, WA, 99164, USA
[d] Department of Physics and Astronomy, Washington State University, Pullman, WA, 99164, USA
[e] Department of Chemistry, Washington State University, Pullman, WA, 99164, USA
[f] Institute for Integrated Catalysis, Pacific Northwest National Laboratory, Richland, WA, 99352, USA
[g] Bioproducts Sciences and Engineering Laboratory, Richland, WA, 99354, USA

ARTICLE INFO

Article history:
Received 19 September 2019
Received in revised form
6 January 2020
Accepted 22 February 2020
Available online 29 February 2020

ABSTRACT

Quantifying the content of surface nitrogen and oxygen containing functional groups in amorphous nitrogen doped carbons via deconvolution of C 1s x-ray photoelectron (XPS) spectra remains difficult due to limited information in the literature. To improve the interpretation of XPS spectra of nitrogen-doped carbons, the C 1s, N 1s and O 1s core level energy shifts have been calculated for various nitrogenated carbon structures via DFT. Furthermore, we propose an expanded method to improve the self-consistency of the XPS interpretation based on a seven-peak C 1s deconvolution (3 C–C peaks, 3 C–N/-O peaks, and π-π* transition peaks). With the DFT calculations, spectral components arising from surface-defect carbons could be distinguished from aromatic sp^2 carbon. The deconvolution method proposed provides C/(N + O) ratios in very good agreement (error less than 5%) with those obtained from total C 1s, N 1s and O 1s peaks. Our deconvolution strategy provides a simple guideline for obtaining high-quality fits to experimental data on the basis of a careful evaluation of experimental conditions and results.

1. Introduction

Amorphous carbon produced from lignocellulosic materials has received much attention in recent years because of its applications in environmental and agricultural management [1], with potential to sequester carbon, serve as a soil amendment, and improve soil aggregation. Modern engineered amorphous carbons with tailored properties, such as porous structure, surface functionalities (O, N, P, S) [2,3] and layers with large number of defects [2,3], are used in the field of adsorption and catalysis [4–8]. There is a growing interest in the production of nitrogen doped carbonaceous materials because of their excellent properties in a variety of applications such carbon electrodes [9], heterogenous catalysis [10–20], adsorption [4–8,21–23], and batteries [24–30]. Nitrogen is typically introduced into chars in two ways: (1) carbonizing nitrogen-containing organic compounds (*e.g.*, melamine [31–33], 3-methyl-1-butylpyridine dicyanamide ionic liquid [34,35]), or (2) treating a carbonaceous material at high temperatures with nitrogen-containing gases which decompose at reactor temperatures, generating highly reactive radicals (for example, using ammonia gas [9,36–38]). These radicals react with the carbonaceous material to form pyridines, pyrroles, graphitic nitrogen, amines, pyridones, and N-oxides. Nitrogen-containing functionalities are responsible for an increase in the surface polarity of carbons [39], and for basicity, since both pyridines and pyrrole-type structures are considered basic [39]. However, in general, the acidic/basic character is governed by the heterogeneity of the nitrogen containing surface groups [40].

X-ray photoelectron spectroscopy (XPS) has been used to

* Corresponding author. Department of Biological Systems Engineering, 2710 Crimson Way, Washington State University, Richland, WA, USA.
** Corresponding author. Voiland School of Chemical Engineering and Bioengineering, Washington State University, 257 Wagner Hall, Pullman, WA, 99164, USA.
E-mail addresses: js.mcewen@wsu.edu (J.-S. McEwen), mgarcia-perez@wsu.edu (M. Garcia-Perez).

https://doi.org/10.1016/j.carbon.2020.02.065
0008-6223/

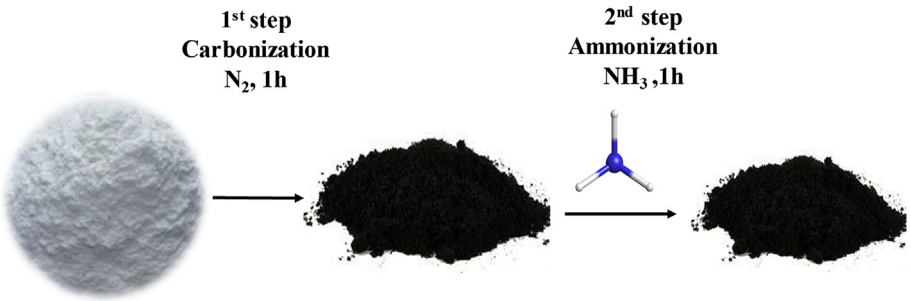

Fig. 1. Illustration of the char produced via ammonia doping. (A colour version of this figure can be viewed online.)

analyze N-doped chars, carbon nanotubes (CNTs), and graphene [41–43], resulting in a wealth of char and graphene related XPS analysis in the literature [28,44,45]. It is a versatile tool that can provide information on the chemical and electronic states on a surface and, within certain limits, on the near-surface region even under reaction conditions [46–48]. The most frequently assigned N 1s peaks are pyridinic (398.2–399.1 eV) [33,49,50], graphitic-N (401.1–402.7 eV) [33,49,50], nitrogen-oxide (402.6 eV) [33,49], amine (400.0 eV) [51], and pyrrolic (400.1–401.2 eV) [52]. In the C 1s region for various carbonaceous materials, peak assignments have been made to C^2_{sp}-C^2_{sp} (284.7–284.9 eV), C^2_{sp}-N (285.3–286.7 eV), and C^3_{sp}-N (286.5–287.7 eV) groups [53].

The lack of accepted methodologies guiding the fitting of XPS spectra is a major concern, where many of the published XPS deconvolution of amorphous carbons being unreliable since they lack a clear guidance to analyze the spectra of interest. Specifically, the quantification of the total oxygen or nitrogen composition obtained from deconvoluting the C 1s spectra does not agree with the values obtained directly from the total C 1s, N 1s and O 1s spectra. Several methods have been proposed in the literature to quantify the oxygen content from oxygenated carbonaceous materials, briefly summarized by Smith et al. [45]. To improve the quantification of oxygen content in the deconvoluted C 1s spectra, Smith et al. proposed a method based on a 7-peak C 1s deconvolution (3 C–C peaks, 3 oxygenated peaks, and π-π^* transition peak), which resulted in C:O ratios in good agreement of those obtained from total C 1s and O 1s spectra.

The lack of reliable methods for the deconvolution of C 1s, N 1s and O 1s XPS spectra is a major challenge for the analysis of these materials. To the best our knowledge no suitable method exists to accurately correlate both the nitrogen and oxygen content to the carbon (C 1s) XPS spectrum in the literature.

Thus, the main aim of this paper is to examine the deconvolution of XPS spectra from N-doped amorphous carbonaceous materials. Here, we consider the influence of defect-related carbon on the core level binding energy as this will provide suitable guidelines for the fitting procedures of the C 1s region. To achieve this, various nitrogenated model compounds and functionalized coronene-based structures were examined using density functional theory (DFT) to predict the core level binding energies of different nitrogen functional groups (C 1s and N 1s). The core level binding of oxygen is presented in a previous publication by our group [45].

2. Methods

2.1. N-doped char production

In this paper N-doped chars were produced by two ways: (1) carbonizing a nitrogen-containing organic compounds (melamine) and (2) treating the char at high temperatures with ammonia gas. A series of N-doped chars were produced by carbonization at temperatures ranging from 350 to 700 °C from cellulose and melamine (cellulose: melamine ratio of 2:1 and 4:1 respectively) in a spoon reactor following the same methods as previously described [45,54,55]. Briefly, the furnace is preheated to a desired temperature while a pre-weighed sample (4.0 g) is stored in a water-jacketed cooling zone. The cooling zone and furnace are purged with a N_2 gas (99%) stream flowing at approximately 300 mL min^{-1} for a minimum of 10 min prior to treatment. At the start of the experiment, the sample is introduced into the furnace and treated for 30 min and 60 min residence times at the required temperature (350–700 °C) before withdrawal to the cooling zone. A secondary preheated nitrogen sweep gas, flowing at approximately 550 mL min^{-1}, is employed in the reactor zone to avoid char oxidation. Samples were allowed to cool to temperatures below 25 °C under N_2 before exposure to air and later stored in sealed containers. The char with a cellulose: melamine ratio of 2:1 and that introduced into the furnace and treated for 60 min was used for the deconvolution analysis in the rest of the paper.

The nitrogen doped char using ammonia was produced through carbonization of cellulose followed by ammonization at a temperature of 350–700 °C(See Fig. 1). This was conducted in a Quartz Tube furnace reactor with 50 mm OD by 44 mm ID at a length of 1000 mm. The carbonization was conducted under an oxygen free atmosphere by purging the reactor with N_2 gas. Briefly, cellulose was kept in a tubular furnace in contact with N_2 for 30 min at 25 °C. Then, the temperature was increased from 25 °C to the desired set temperature at a heating rate of 10 °C min^{-1}. The reactor was then kept at the set temperature for 2 h. In the first hour, cellulose was pyrolyzed to char under a N_2 gas environment. Following the carbonization, the resulting char was treated with ammonia for one additional hour. Flow rates of 500 mL min^{-1} for N_2 and 1000 mL min^{-1} for ammonia were employed. The final char produced was cooled down to 25 °C under N_2 gas before storage and characterization.

2.2. Char characterization

2.2.1. Elemental analysis

Elemental analysis was performed using a TRUSPEC-CHN® elemental analyzer (LECO, U.S.). Briefly, 0.15 g of sample was used to determine the total carbon (C), nitrogen (N) and hydrogen (H) contents. The oxygen (O) mass fraction was determined by subtracting the ash, C, N, and H contents from the total mass of the sample.

2.2.2. Proximate analysis

Moisture, fixed carbon, volatile matter, and ash content in all chars produced were determined using a thermogravimetric analyzer, SDTA851e (Mettler Toledo, U.S.). The percentage of fixed carbon was determined by subtracting the ash percentage from the

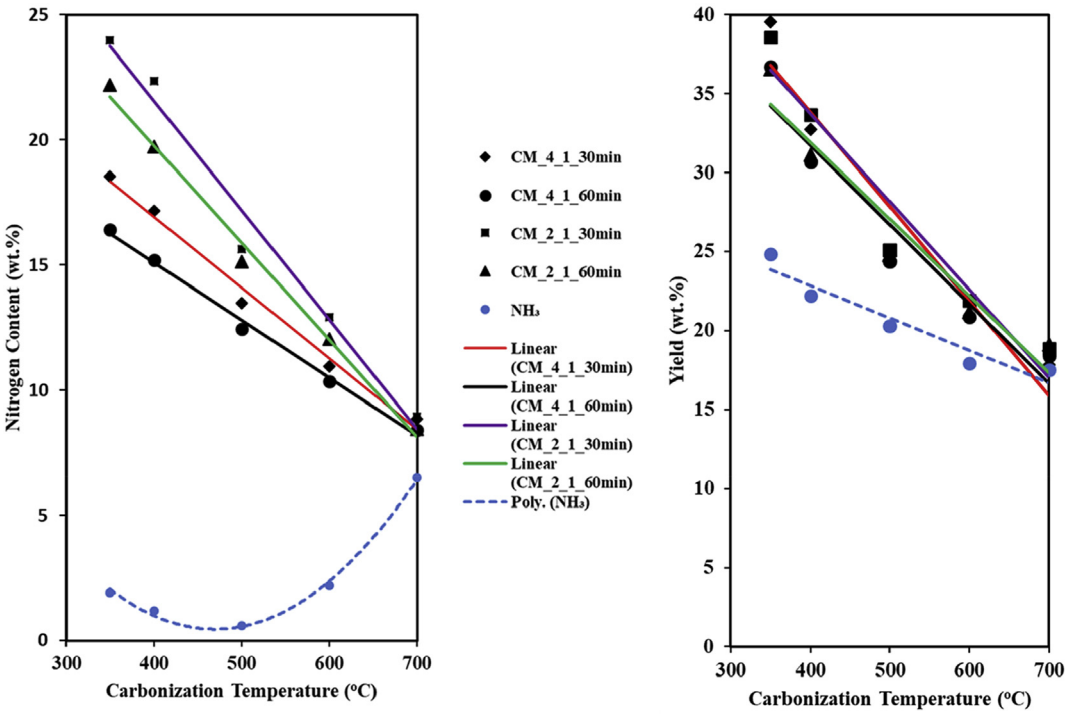

Fig. 2. Nitrogen content (a) and Yield of product (b) obtained using different ratios of cellulose-melamine mixture (CM) or ammonia activation (NH_3) at varying residence times and temperatures. (A colour version of this figure can be viewed online.)

volatile matter percentage, after assigning all weight loss up to 120 °C to loss of free and non-structural water.

2.2.3. Fourier transform infrared spectroscopy (FTIR)

FTIR spectra were obtained using a Shimadzu IRPrestige 21 spectrometer equipped with MIRacle single reflection ATR Ge probe. The char samples were placed to cover the crystal window, and the spectra acquired with (64 scans, 600–4000 cm^{-1}, and a resolution of 4 cm^{-1}).

2.2.4. X-ray photoelectron spectroscopy

XPS analysis was performed using an AXIS-165 upgraded to an Ultra manufactured by Kratos Analytical Inc. Achromatic X-ray radiation of 1253.6 eV (MgKα) was used to analyze each material. All high-resolution spectra were recorded using a pass energy of 40 eV and spot size of approximately 120 μm. The spectrometer was calibrated against both the Au $4f_{7/2}$ peak at 84.0 eV and the Ag $3d_{5/2}$ peak at 368.3 eV. The minimum full width at half maximum (FWHM) for the Au $4f_{7/2}$ peak is approximately 0.85 eV, representing the absolute minimum possible broadness achievable for this configuration. Survey scans have been obtained using a pass energy of 80 eV and step sizes of 1 eV to determine the overall chemical composition of each sample. To determine the speciation of carbon, nitrogen and oxygen groups, high resolution scans of the C 1s, N 1s and O 1s regions (280–295, 394–404 and 527–538 eV, respectively) were collected for each material using 0.1 eV step sizes. Static charging was detected in chars produced at temperatures less than 500 °C. This charging was corrected with a neutralizer (flood gun) by centering the C–C peak near 284.7 eV.

2.3. Computational details

The core level binding energies of both C 1s and N 1s were obtained from the orbital energies using the modified Koopmans theory package within Gaussian 09. The Becke three-parameter Lee-Yang-Parr (B3LYP) hybrid functional and a 6-311G(p,d) basis set [56] was used to perform the geometry optimization. To calculate the C 1s XPS spectra, a linear correction factor was used ($BE_{corrected} = BE_{B3LYP}$ (eV)*0.9698 + 19.94) [45]. We note that this estimate does not take into account the electron rearrangement, but has been found to provide a reasonable estimate for the binding energies using this simple linear correction factor. Using this linear equation, a deviation of more than 0.40 eV from the average calculated binding energy of a coronene structure (284.6 eV) was considered significant for this study [45]. Model compounds such as acridine, aminoanthracene, carbazole, and melamine have been analyzed to confirm the validity of the computational method presented here. The linear correction factor used for the C 1s spectra is not valid for the N 1s spectra. As such, for the simulation of the N1s XPS spectra, a scaling factor of 1.038, obtained from dividing the experimental value of acridine (398.8 eV) by the calculated value of acridine (384.03 eV), was multiplied to all of calculated binding energies to compensate for the difference between the calculated values and experimental values [57,58]. Several defects, including nitrogenated functional groups, were created on the coronene structure to evaluate the effects of various carbon bonding structures proposed to be predominant in the chars and the likely shifts associated with both the C 1s and N 1s core level binding energies [54]. We also estimated the binding energy of oxygen when bonded to nitrogen as found in nitrogen oxides, where water was used as the reference structure. Using the information obtained from the DFT-based calculations, such as the peak position, the deconvolution process of the char was realized in an in-house excel based routine to enable us better to tune the fitting parameters, such as the asymmetry factor (TS), the asymmetric tailing factor (TL), and the G-L ratio. We also calculated the C 1s core level binding energies shifts for larger, periodic systems using the Vienna Ab Initio Simulation Package (VASP) [59–61], where we find that the core level binding energy shifts of the C–N models compare well to the results obtained using Gaussian software for

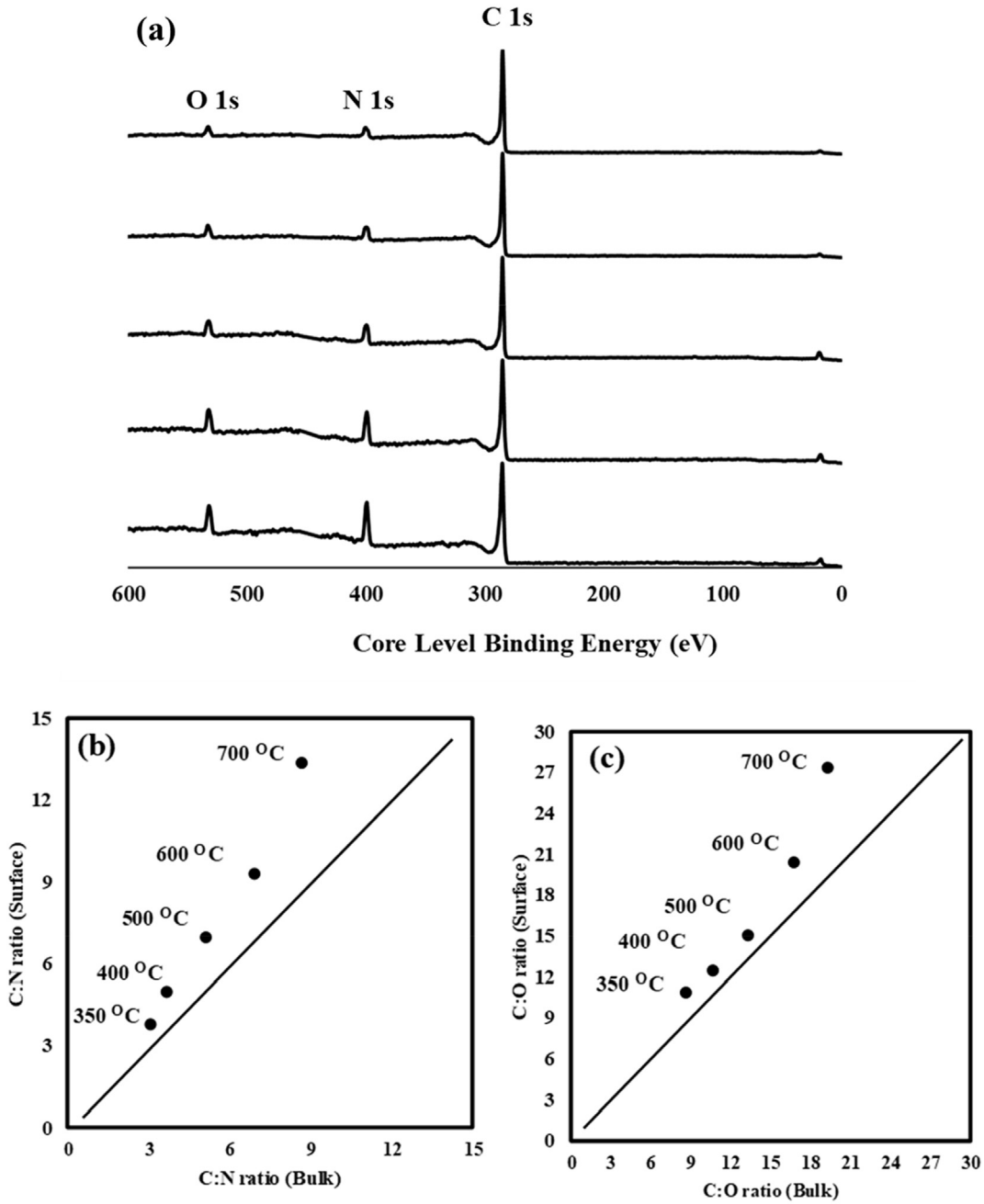

Fig. 3. (A) The full XPS survey scan of chars treated at various temperatures from a mixture of cellulose and melamine. (B) Parity plots for the surface vs bulk C:N ratios and (b) the C:O ratios (c) ratios. The surface ratios were obtained from the XPS results shown in Table 2, while the bulk quantities were obtained from LECO elemental analyzer (Table 1).

smaller systems that are presented in this manuscript (see Supporting Information for more details of larger systems, Figs. S1—S3 and Table S1).

3. Results and discussions

3.1. Production and characterization of amorphous carbonaceous materials

Fig. 2 presents the yield of char, the nitrogen content, the cellulose to nitrogen-precursor ratio, and the effect of temperature in the presence of ammonia. The yield of char decreased with increasing temperature, which is due to the loss of volatiles by the pyrolysis reactions [62,63]. Char produced from a mixture of cellulose and melamine (CM) has a higher char yield than that produced with ammonia gas. However, both treatment species present a similar decreasing trend with increasing temperature, and all yields converge to roughly the same value at 700 °C. The high yield of CM char might be due to the fact that the mixture of melamine and cellulose increases the chance of cross-linking reactions [64] and collision of different compounds leading to secondary char forming reactions.

While melamine and ammonia treatments show similar trends in terms of yield, they behave very differently when it comes to nitrogen content. The nitrogen content of the CM chars decreased fairly linearly from 350 to 700 °C. Regardless of the cellulose,

Table 1
Bulk and surface elemental composition of nitrogenous char. Bulk elemental analysis data is on dry basis.

Samples	CM350[a]	CM400	CM500	CM600	CM700
C(wt.%)	62.3	66.6	74.3	77.6	82.2
H(wt.%)	3.9	3.4	2.4	1.7	0.9
N(wt.%)	24.1	21.6	17.1	13.2	11.1
O(wt.%)	9.7	8.4	7.5	6.2	5.7
Ash(wt.%)	<0.1	<0.1	<0.1	<0.1	<0.1
C:O[a]	8.6	10.6	13.2	16.7	19.2
C:N[a]	3.0	3.6	5.1	6.9	8.6
C/(N + O)	2.2	2.7	3.7	4.9	6.0

[a] Molar, dry ash free.

Table 2
High resolution scan parameters. Surface composition was obtained by XPS via integrated areas of the high-resolution scans, considering the instrument's sensitive factors (SF) (see method section for SF of C, N and O).

Fine Scan Total peak areas	CM350[a]	CM400	CM500	CM600	CM700
C 1s (counts/sec)	17414	14570	21620	34284	30002
N 1s (counts/sec)	7846	4975	5298	6300	3837
O 1s(counts/sec)	4517	3274	4045	4713	3078
C (at. %)	73.8	78.2	82.7	86.5	90.0
N (at. %)	19.4	15.6	11.8	9.3	6.7
O (at. %)	6.8	6.3	5.5	4.2	3.3
C:N	3.8	5.0	7.0	9.3	13.4
C:O	10.8	12.5	15.0	20.4	27.3
C/(N + O) ws	2.8	3.6	4.8	6.4	9.0

ws (wide scan).
[a] CM350-700 (Cellulose nitrogen doped and Production temperature).

melamine ratio and residence time, all CM chars produce a fixed amount of stable nitrogen at 700 °C. When using ammonia for the treatment the content of nitrogen first decreased from 350 to 500 °C before suddenly increasing from 500 to 700 °C to approach the nitrogen content of the CM chars. The ammonia reacted with the char only at temperatures over 500 °C. These results clearly indicate that the amount of nitrogen in the structure of chars varies widely depending on doping agent precursor and production conditions.

3.2. Experimental XPS results

Fig. 3a shows a full survey of scans for the XPS signal up to binding energies of 600 eV. The results show that only carbon, nitrogen, and oxygen contribute significantly to the surface chemistry. The quantification of these elements was obtained by applying a Shirley type background correction to each peak and applying the pertinent sensitivity factors (SF) to standardize the reported counts/sec. The instrument-specific sensitivity factors used for carbon, nitrogen, and oxygen are as follows: 0.278, 0.477, and 0.780 respectively. It is observed from the full survey scan that the surface carbon content increases with the production temperature, whereas both the nitrogen and oxygen content decrease as the temperature rises as a result of volatilization and polycondensation reactions [63,65]. These results agree well with the bulk elemental composition analysis shown in Table 1 and Table 2. In the parity plots of the C:N and C:O ratios from the bulk and surface elemental composition analysis, as shown in Fig. 3b and c. There is increasing divergence as the carbonization temperature increases above 500 °C. In most cases the oxygen content on the char surface is more than the bulk due to post-secondary oxidation when exposed to air — higher temperature char production leaves the surface of the char with highly active sites acting as free radicals and upon cooling can react with oxygen or water/moistures in the environment [66,67].

As we are interested in deconvoluting the XPS spectra, collecting high-resolution spectra for the C 1s, N 1s and O1s signals is necessary to discern the bonding states between carbon, nitrogen and oxygen. Fig. 4a shows the C 1s spectra as a function of char temperature of N-doped char. A broad peak centered at 285.0 eV is

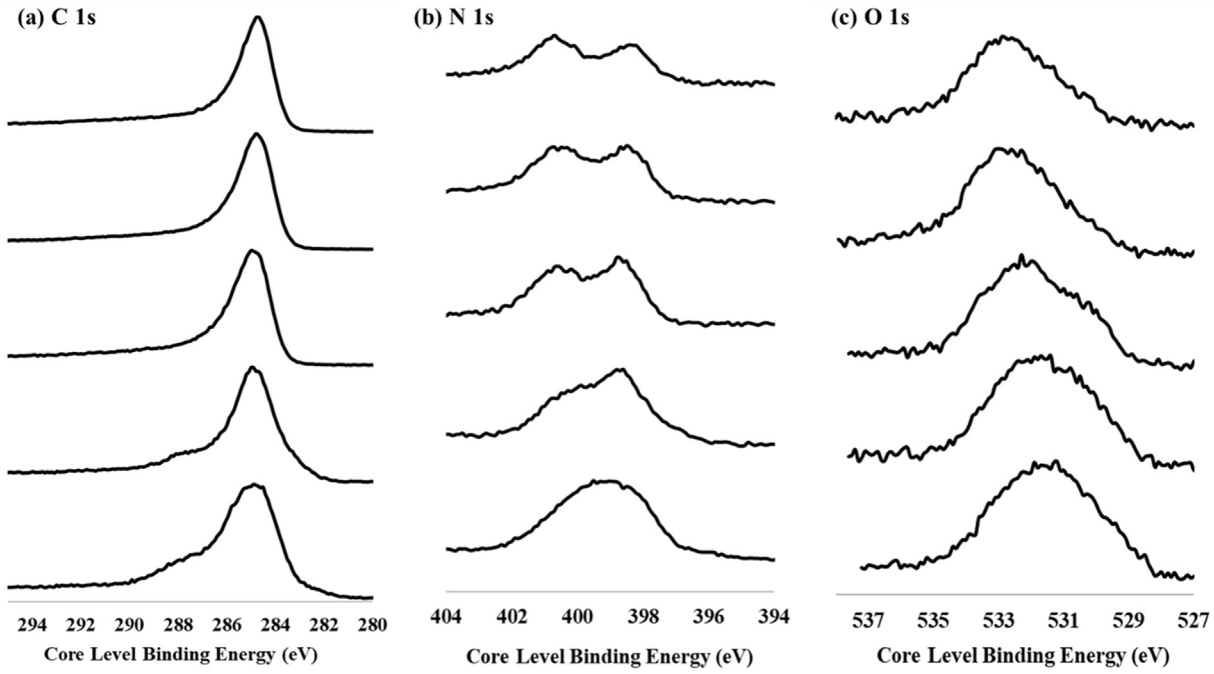

Fig. 4. High resolution scan of (a) C 1s, (b) N 1s and (c) O 1s XPS spectra for nitrogenated char (CM_2:1_60min) as a function of carbonization temperature.

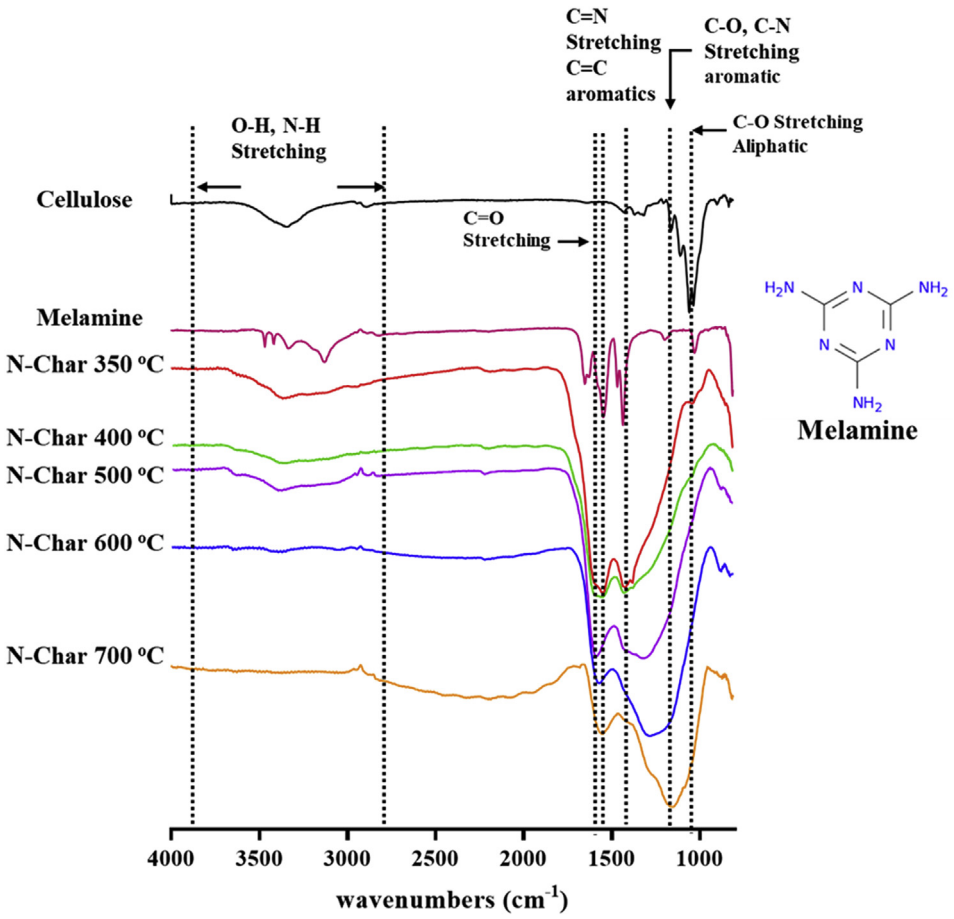

Fig. 5. FTIR of N-doped char (CM char) produced at different temperatures between 350 and 700 °C. (A colour version of this figure can be viewed online.)

observed at lower temperatures (350–400 °C) with a shoulder peak prominent at near 287.0–288.0 eV. As the temperature is increased to 700 °C, the 285.0 eV peak at 300 and 400 °C narrows and shifts to 284.7 eV and the peak near 288 eV disappears because of the loss of both oxygen and nitrogen functional groups and the polycondensation of aromatic structures. For the N 1s high resolution spectra, a clear trend in the evolution of functional groups can be seen as the temperature rises from 350 to 700 °C, as shown in Fig. 4b. At 350 °C, a broad peak centered at 399 eV is observed, where the broadness is likely due to the highly amorphous nature of char produced at lower temperatures (see the XRD test results in the Supplementary Information as Fig. S4). A clear definition of specific functional groups starts to appear as the temperature is raised to 400 °C with a sharp peak appearing at 398.8 eV and a shoulder emerging at 400 eV. Increasing the temperature further from 500 to 700 °C shows the nitrogen forming two main functional groups with binding energies at 398.8 and 400.7 eV. These two main peaks situated at 398.8 and 400.7 eV are experimentally assigned to pyridinic and pyrrolic functional groups, respectively [50,68]. This assignment is supported by molecular modeling in the literature [57,69,70] and in this present study. The O 1s peak is partially symmetric, where the maximum peak distribution is shifted toward higher binding energies at about 533 eV as the carbonization temperature increases. This binding energy is related to ether and hydroxyl groups bonded to aromatics [45]. However, since our FTIR test doesn't shows any presence of hydroxyl functional groups at higher temperatures (600–700 °C) we consider that shift toward higher energy values may be related to stable ether functional groups.

The bulk composition results were confirmed by FTIR (see Fig. 5). From the spectra obtained for the different chars, relatively intense and distinct peaks were observed. Bands between 3723 and 3176 cm^{-1} were assigned to –OH and N–H functional groups. A low intensity broad peak was observed within this range for char produced at 350 °C, 400 °C and 500 °C which was attributed to an –OH group. This group disappears as the temperature increases from 400 to 700 °C. No bands were found at ~2270 cm^{-1} which is normally assigned to C≡N functional group. The peaks between 1680 and 1400 cm^{-1} were characteristic bands of C=O and C=C (aromatic structures) and C=N/C–N, respectively. The broadness depicted might be due to the convolution of all these bonds. The bands at around 1071 cm^{-1} were attributed to C–O–C stretching in aromatics. This analysis is relevant as it supports the elimination of amines and nitrile groups in the deconvolution of the nitrogen XPS spectra.

3.3. Benchmarking DFT-based XPS spectra

We have benchmarked our DFT calculated XPS spectra by comparing theoretically and experimentally determined XPS spectra for several reference model compounds (acridine, aminoanthracene, carbazole, and melamine). In order to generate spectra from each DFT calculated binding energy and its corresponding intensity for its comparison to experimental spectra, a Gaussian:-Lorenztian sum (G:Lsum) function (see equation (1)) was used. To optimize these parameters, the G:L distribution and the full width

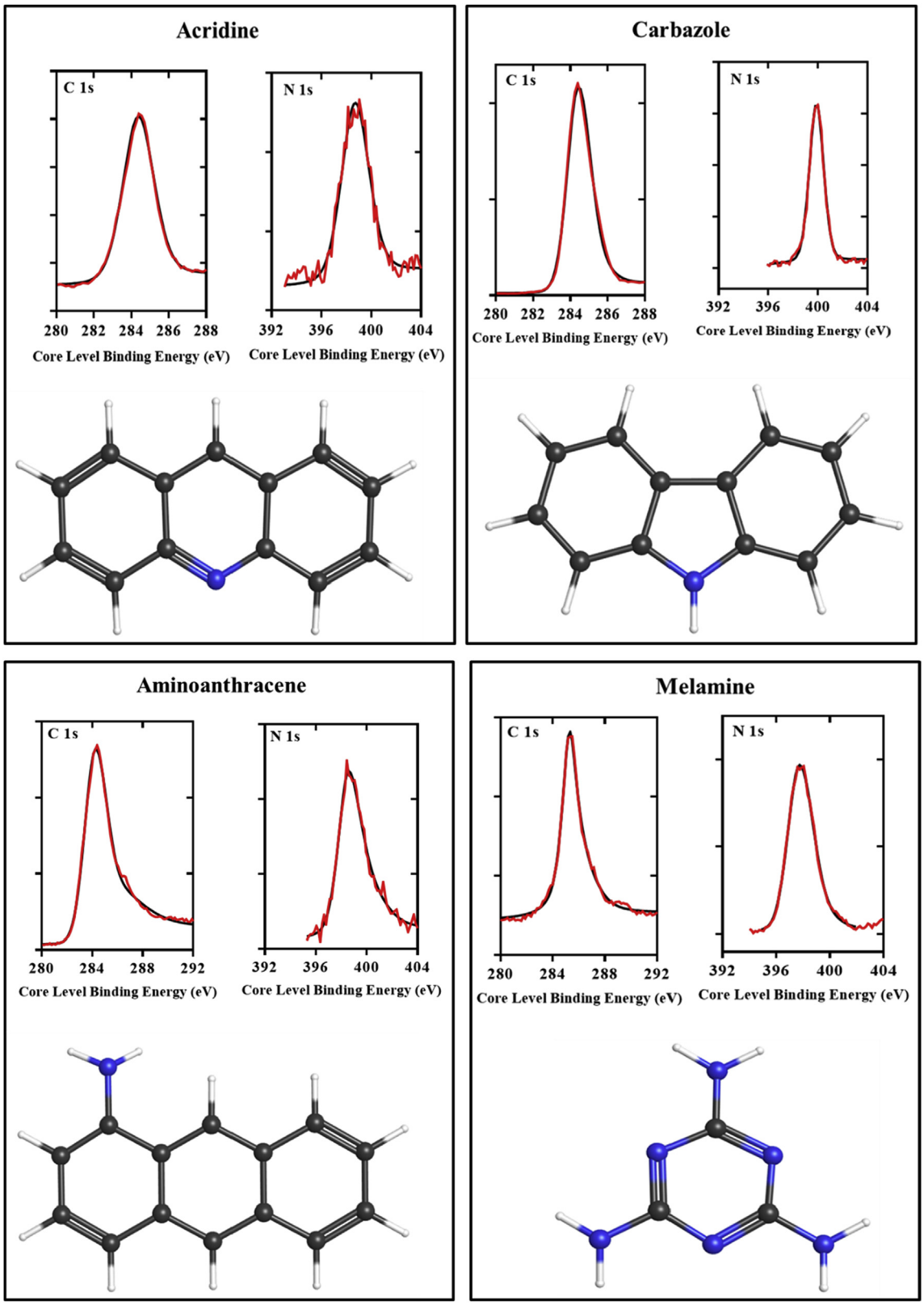

Fig. 6. Experimental (red) and DFT calculated (black) XPS spectra for the C 1s and the N 1s core level binding energies. The black, blue, and white spheres represent carbon, nitrogen, and hydrogen atoms, respectively. (A colour version of this figure can be viewed online.)

Table 3
Core level energy shift of different model compounds (C directly bonded to N). The experimental N 1s core level binding energies are also presented.

Model compounds	C 1s			N1s		
	Exp. C–C peak (eV)	DFT calculated C 1s -(N) shifts (eV)	DFT C–N peak position (eV)	Exp. (eV)	DFT calculated N 1s -(C) shifts(eV)	DFT N 1s-(C) peak (eV)
Acridine	284.4	1.1	285.7	398.7	0.0(ref)	398.8
Carbazole	284.4	1.1	285.7	399.9	1.9	400.7
Amino-anthracene	284.3	1.1	285.7	399.6	0.8	399.8
Melamine	284.3	2.9	287.5	397.8[a]	0.0	398.8[a]
				399.6[b]	1.0	399.8[b]

[a] Pyridinic group and.
[b] Amine group in melamine compound.

at half maximum (FWHM) as well as the TS and TL were allowed to relax to the optimum fitting value. Below is the G:Lsum function used in this study. A more general form of this equation can be found elsewhere [45].

$$\mathbf{GLsum} = \mathbf{h} \times \left((1-\mathbf{m}) \times \boldsymbol{e}^{-\boldsymbol{ln}(2)\times\left[\frac{2\times(\boldsymbol{x}-\boldsymbol{p})}{\boldsymbol{W}}\right]^2} + \frac{\boldsymbol{m}}{1+\left[2\times\frac{\boldsymbol{x}-\boldsymbol{p}}{\boldsymbol{w}}\right]^2} + \boldsymbol{TS}\left[1-\boldsymbol{e}^{-\boldsymbol{ln}(2)\times\left[2\times\frac{\boldsymbol{x}-\boldsymbol{p}}{\boldsymbol{w}}\right]^2}\right] \times \boldsymbol{e}^{-\frac{6.9}{\boldsymbol{TL}}\times\left[2\times\frac{\boldsymbol{x}-\boldsymbol{p}}{\boldsymbol{w}}\right]^2} \right) \quad (1)$$

x = binding energy (eV), p = peak center (eV), w = FWHM (eV), m = Gaussian-Lorentzian mixing (0 Gaussian: 1 Lorentzian), h = peak height (counts/sec), TS = asymmetry parameter, and TL = asymmetry tailing parameter.

The results of DFT and experimental spectra of the reference systems are shown in Fig. 6 and in Table 3. Table 4 presents the resulting fitting parameters obtained as a result of matching the DFT binding energies (via equation (1)) to the experimental data of the model systems. The fitting of XPS spectra does not only depend on peak position but also fitting parameters such as the line shape, asymmetric factor (TS), and the asymmetric tailing (TL) [71].

The C 1s energy shift and binding energy for C–N relative to the graphitic C–C peak of coronene (C–C peak of coronene, which is here referred to as graphitic due to the planar hexagonal ring structure of the system and to distinguish it from non-hexagonal and non-planar defects), as well as the N 1s energy shift and peak position (given both for the calculated and the experimental peak position), are shown in Table 2. Surprisingly, the carbon bonded to nitrogen in a six-member ring (acridine) has the same C 1s core level energy shift (1.1 eV) as that bonded to nitrogen in a five-member ring (carbazole) or to aminic nitrogen (amino-anthracene). Additionally, the carbon bonded to 3 nitrogen atoms (melamine) presents a shift of 2.9 eV relative to graphitic carbon. Melamine has two nitrogen functional groups with theoretical binding energies of aminic (399.8 eV) and pyridinic (398.8 eV) functional groups. Pyrrolic functionality can be found in the structure of carbazole with a calculated binding energy of 400.7 eV.

From Table 3 and Fig. 6, the N 1s core level binding energies compare very well with both the experimental energies and the spectra, respectively.

3.4. DFT simulation of the C 1s XPS spectra of unknown structures

The fundamental problem always faced in XPS deconvolution analysis of functionalized amorphous carbons is the C 1s position when bonded to different types of nitrogen functional groups and other heteroatoms. To achieve a better understanding of the C–N peak position apart from the simple reference compounds (Fig. 6), we calculated the energy shift of unknown nitrogenated structures. Fig. 7 presents the simulated C 1s XPS spectra of different nitrogen functional groups introduced in a coronene molecule. Generally, the degree of C–N core level binding energy shift relative to the C–C peak is determined by the type of hybridization. For example, C^2_{sp}-N (Fig. 7a–d) shows an energy shift ranging from 1.0 to 1.4 eV while C^3_{sp}-N (Fig. 7c and d) ranges from 1.8 to 1.9 eV. Other factors such as ring strain and vacancies also influence the core level binding energy value. Fig. 7a shows a pyrrolic group, and the binding energies of the carbons in the five-member ring (C_b and C_c) have a core level binding energy shift of −1.1 eV. We thought initially that the nitrogen in the five-member ring might have altered the electronic configuration of

Table 4
Fitting parameters used for the analysis of model compounds with a G:Lsum line shape.

Samples	C 1s				N1s			
	FWHM	G-L (0–1)	TS (0–1)	TL (1–200)	FWHM	G-L (0–1)	TS (0–1)	TL (1–200)
Acridine	2.0	0.2	0.0	0.0	2.4	0.2	0.0	0.0
Carbazole	1.4	0.1	0.2	32	1.4	0.2	0.0	0.0
Amino anthracene	2.0	0.1	0.3	114	1.9	0.3	0.4	55
Melamine	1.4	0.8	0.3	65	2.0	0.0	0.3	35
Average Parameters	1.7	0.3	0.2	52.8	2.0	0.2	0.2	22.5

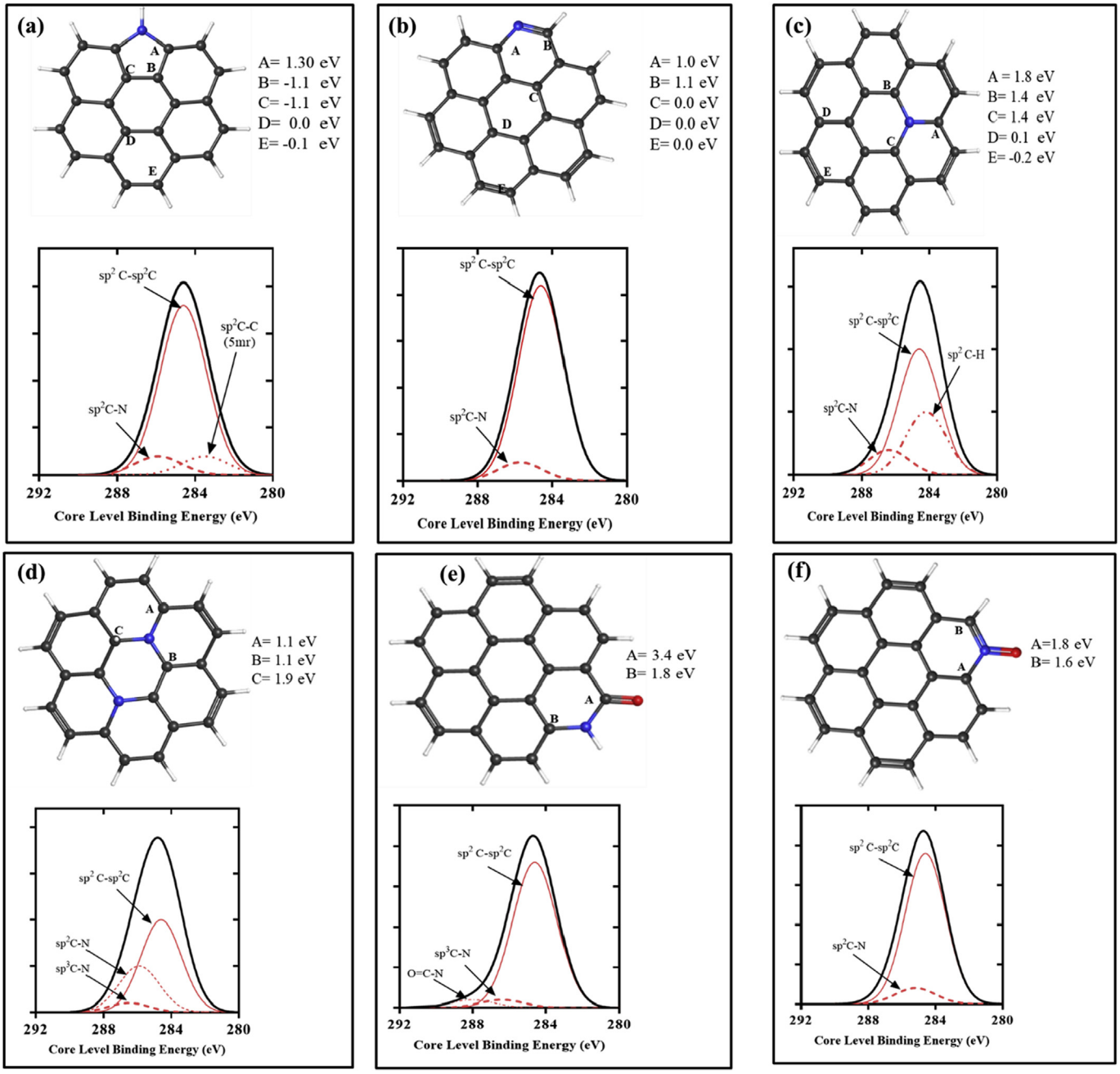

Fig. 7. Structures with different nitrogen functionalities in coronene with the corresponding DFT calculated C 1s spectra: (a) pyrrolic, (b) pyridinic, (c) graphitic, (d) two graphitic nitrogen in para position, (e) pyridone, and (f) N-oxide. Sphere colors are the same as in Fig. 5, with the red sphere representing oxygen. Labels A-F are the core level binding energy shifts of C 1s relative to coronene. (A colour version of this figure can be viewed online.)

the ring relative to a six-member ring. However, this hypothesis contradicts our findings on the study of the stability of nitrogenated carbon materials through DFT where we found that nitrogen functionalization of a hydrogen terminated graphene edge does not significantly affect the edge's electronic structure [72]. Nonetheless, studies on the effect of an internal cyclopentane ring within a polyaromatic structure shows that the core level binding energies for carbon atoms in the cyclopentane systems reveals a downshift of 0.57 eV as compared to the average C 1s core level binding energy of coronene [45]. This downshift might be the reason behind the observed distinct asymmetry on the low binding energy side of the carbon spectra. The possibility of bonding states between oxygen and nitrogen was also considered, revealing a higher C 1s shift of about 3.2 eV for carbon when bonded to both simultaneously (O═C—N in Fig. 7e). Additionally, C—N═O, as present in N-oxides (see Fig. 7f), has a C 1s core level binding energy shift that ranges from 1.6 to 1.8 eV. These calculated C 1s core level binding energy shifts can be used to predict the peak position of each functional group and hence facilitate the deconvolution of any carbonaceous material.

In addition to the nitrogen functionality, chars can contain carbon defects, such as vacancies and non-hexagonal structures, as shown by Smith et al. [54]. This gives us the opportunity to test the effect of defects on the core level binding energy shifts in the C 1s spectra of N-doped char (see Fig. 8). Creating a double carbon vacancy and introducing a pyrrolic functionality in coronene (Fig. 8a)

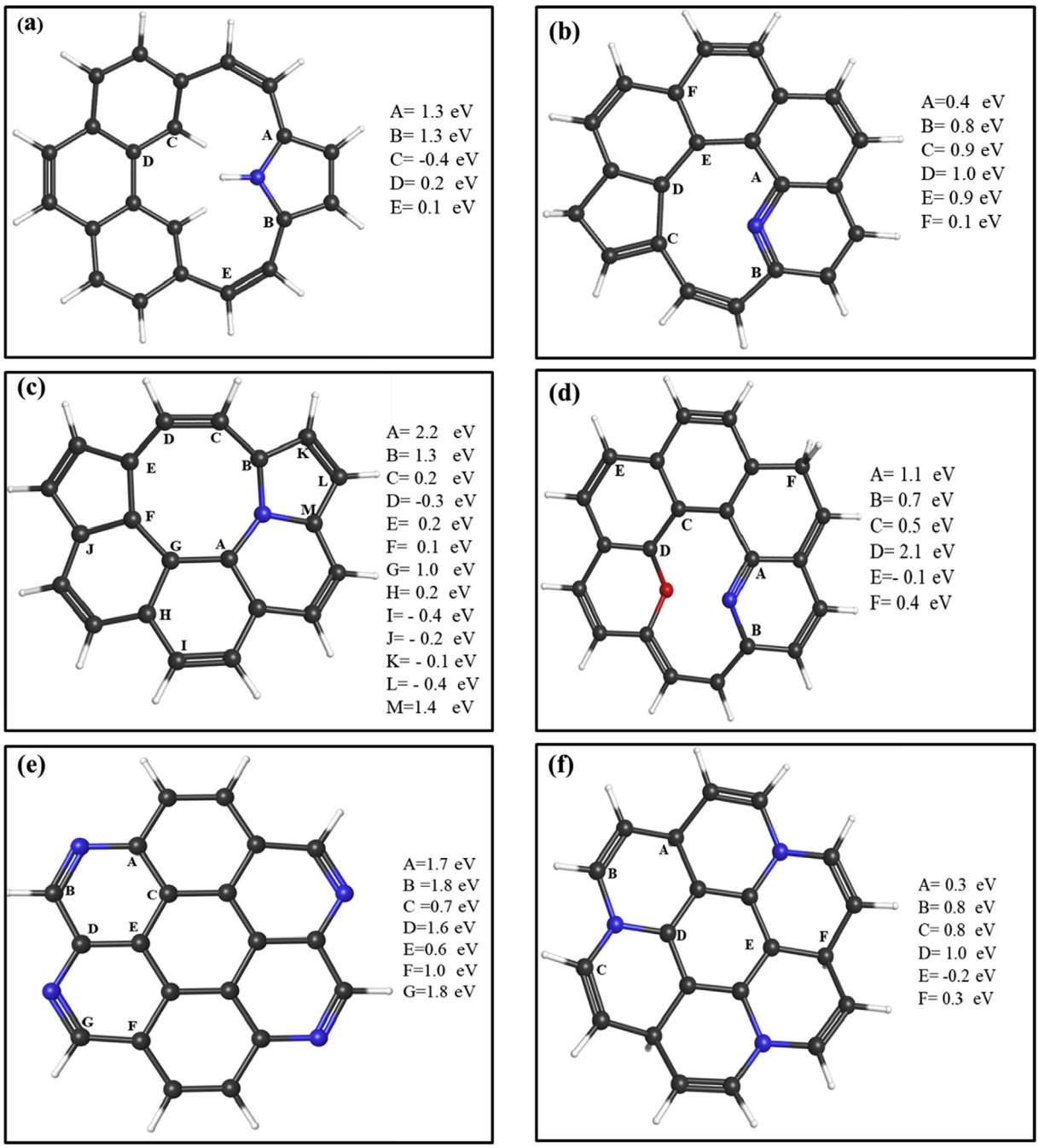

Fig. 8. C 1s core level binding energy shift of carbon defective structures. Labels A-F are the core level shifts of the C 1s core level binding energy relative to coronene. Sphere coloring is identical to Figs. 5 and 6. (A colour version of this figure can be viewed online.)

did not significantly change the core level binding energy shift of the carbon bonded directly to nitrogen, however, it did decrease the C 1s core level binding energy of the edge carbons by −0.40 eV. This is not considered significant due to the error range introduced by the linear equation used to calculate the core level binding energies (see the computational details section). Fig. 8b shows that a N-doped non-hexagonal structure significantly increases the C 1s core level binding energies of the carbon atoms along the edge. This indicates that C–C adjacent to carbon defects can alter the C 1s core level binding energies in the C–N range (285.7–286.5 eV), contributing to the difficulty in deconvoluting XPS spectra of nitrogenated char. However, the C directly bonded to N on the pyridinic group experienced a decrease in energy by 0.3–0.6 eV as compared to a defect free pyridine model (see Fig. 8b). The effect of a saturated nitrogen edge was investigated by introducing four pyridinic groups to coronene, as shown in Fig. 8e. All the carbons in the ring showed an increase in the C 1s core level binding energies, presenting us with an upper bound during optimization and deconvolution of the C 1s XPS spectra. Fig. 8c and f shows the change in C 1s core level binding energies for graphitic nitrogen in different forms. The core level binding energy shifts calculated for C^{2}_{sp}-N slightly increase in energy in the range of 0.8–1.4 eV when compared to defect free pyridinic and pyrrolic functional groups in Fig. 8a–b. The same is also observed for the carbons with C^{3}_{sp}-N

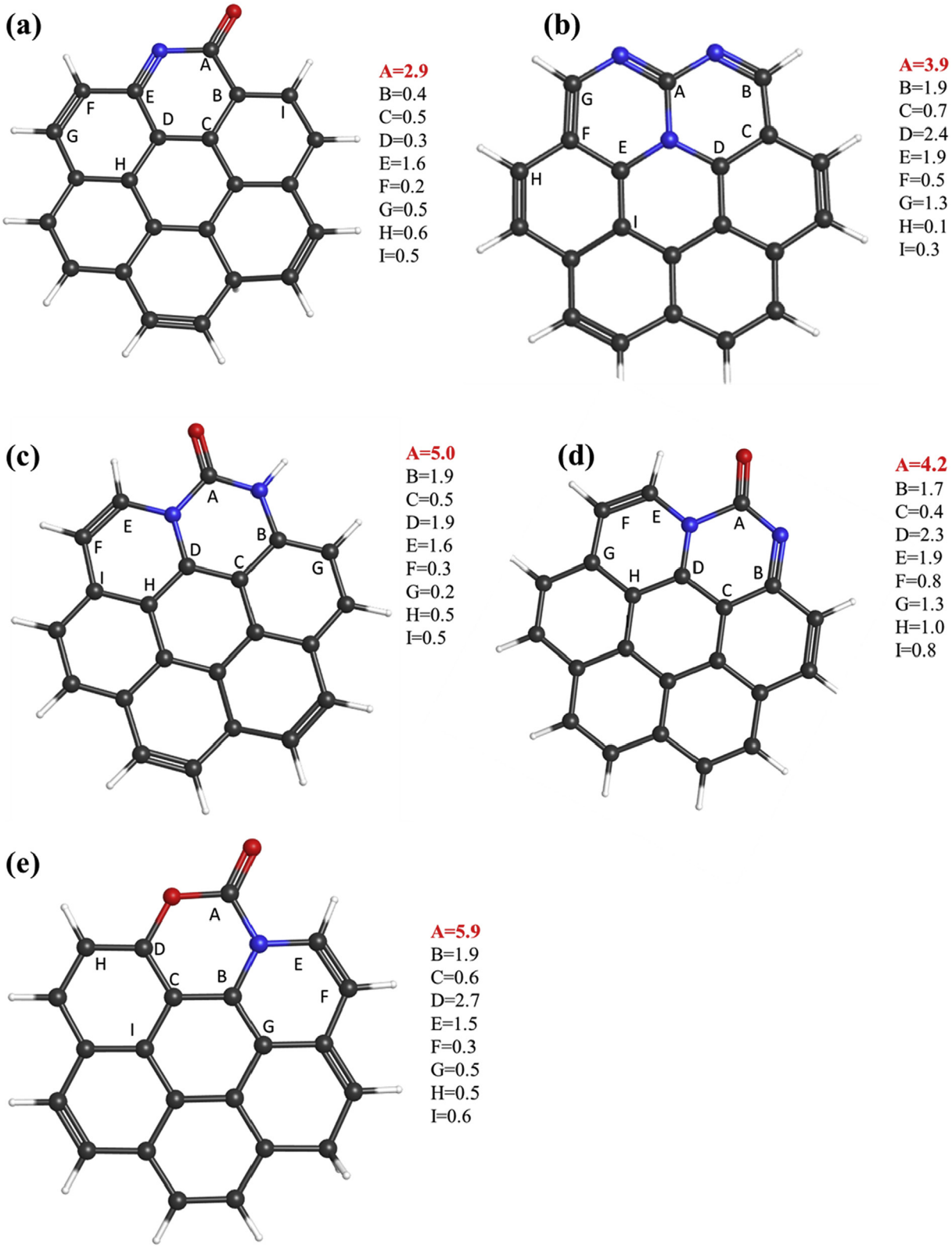

Fig. 9. More structures that benchmark the effect of heteroatoms on the core level binding energy of a modified coronene based model. Labels A-E are the core level shifts of the C 1s core level binding energy relative to coronene. Sphere coloring is identical to Figs. 5 and 6. (A colour version of this figure can be viewed online.)

Table 5
Summary of peak assignments and parameters with the corresponding core level binding energy (CLBE) value range for the interpretation of N 1s and C 1s spectra of chars.

Peak	Assignment	CLBE (eV)	FWHM (eV)	G-L (0–1)
C=N–C	Pyridinic group in aromatics	397.8–398.8	1.4–2.0	0–0.20
C–(NH)–C	Pyrrolic group in aromatics	399.9–400.7	1.4–2.0	0–0.20
C-(NC)–C	Graphitic Nitrogen in aromatics	401.2–401.8	1.4–2.0	0–0.20
O=N–C	Nitrogen Oxides	402.2–404.2 534.0–534.8	1.4–2.0	0–0.20
O=CNC/H–N–H	Pyridone/amine group	399.6–399.9	1.4–2.0	0–0.20
C-C_{low}	Defective carbons in five-member rings	283.2–284.1	1.2–2.0	0–0.30
C-$C_{primary}$	Graphitic carbon	284.3–284.8	1.2–2.0	0–0.30
C-C_{high}/C_{sp2}-N	Carbon in more than six-member ring/Carbon bonded to N in pyridinic, pyrrolic in both defect and defect free regions	284.8–285.5	1.2–2.0	0–0.30
C–O/C_{sp3}-N/C–N=O	Ether ground found in esters and lactone/Graphitic Nitrogen in aromatics/Nitrogen Oxides	285.9–286.5	1.4–2.4	0–0.20
C=O/N-(C_{sp2} = O)/N–C(O)–C	Pyridone, amide/Carbonyl groups	286.5–287.6	1.4–2.4	0–0.20
C(O)–O/N–C(N)–N/N–C(O)–N	Carboxyl, esters, lactone and other related carbons bonded to 2 and 3 heteroatoms	288.4–288.9	1.4–2.4	0–0.20

hybridization, which shows an increase in energy in the range of about 2.2 eV when compared to the graphitic nitrogen structure (see Fig. 8c). Finally, the combined effects of oxygen and nitrogen functionalities within the same carbon-defective coronene were examined via the introduction of both ether and pyridinic groups (Fig. 8d). Smith et al. [73] studied the structure of char using a cross polarization pulse sequence with long range dipolar dephasing and demonstrated that a distribution of ether groups and defects occurs within clusters. Interestingly, the C 1s core level binding energy shift for C^2_{sp}-O (2.0–2.1 eV) was found to be in the same range as that of C^3_{sp}-N in defective structures. This might explain the broadness of the C 1s spectra (Fig. 4a) and the difficulties experienced with its deconvolution. We also calculated the C 1s core level binding energies of larger, periodic systems and the results are consistent with the coronene results (see Supporting Information, Fig. S1 and Table S1).

In addition to the structures tested initially, it is worth testing the effect of multiple bonds on the core level binding energy. For example, N–C(C)–O, N–C(N)–O, N–C(O)–O as well as N–C(N)–N (see Fig. 9). These core level binding energy shifts were calculated with reference to the coronene structure. Structure b and d are noted to have binding energies in the same range of C(O)–O (288.4–288.9 eV) (found in carboxylic, esters and lactones). While natural and synthetic compounds may be expected to show high concentrations of such bonds, given the high temperature, uncontrolled reactions occurring during pyrolysis, it is expected that these bonds will exists based on statistical distributions throughout the structure. Because of these carbons bonded to two or more heteroatoms that are not strongly favored by thermodynamics, these structures (carboxyl/lactone groups) are not expected to contribute strongly to the overall spectra. Hence, these systems have not been considered in the expressions found in the SI for the deconvolution analysis.

3.5. New deconvolution rules for N-doped char

After carefully analyzing the DFT calculated peak positions of both the reference systems and unknown structures as well as the optimum fitting parameters obtained from the reference systems by fitting their DFT-based core level binding energies via equation (1) to their corresponding experimental data, we have been able to establish general rules to deconvolute the XPS spectra of nitrogenated char. We note that the deconvolution scheme proposed is based on the best information available in today's literature and on our DFT molecular modeling studies, but inevitably, the physical picture that will be obtained from the deconvolution of XPS spectra of amorphous carbonaceous materials containing thousands of polyaromatic molecules will always be an approximation based on the information at hand. The fitting scheme proposed cannot be considered final. The authors are aware that it may be expanded or modified with new peaks as new information on XPS secondary effects become available.

Table 5 shows a summary of the peak position, FWHM, and G-L of different C–C, C–N and C–O bonds used here to deconvolute carbon, nitrogen and the oxygen spectra. Different defects on coronene, such as vacancies and non-hexagonal rings, led to the identification of different types of C–C bonds: (1) C–C bond (283.5–284.1 eV) found in pentagonal rings, (2) C–C bond (284.3–284.7 eV) present in graphitic carbon. These findings agree with our previous results [45]. Besides the C–C bond, we also determined the C 1s core level binding energies for 3 distinct types of C–N/(-O) bonds: (1) C^2_{sp}-N (285.1–285.5 eV), (2) C–O/C_{sp3}-N/C–N=O (285.9–286.5 eV), and (3) C=O/N-(C_{sp2} = O)/NC(O)C (286.5–287.6 eV). Both oxygen and nitrogen have a large impact on the core level binding energy of carbon. Carbon bonded simultaneously to oxygen and nitrogen (see Fig. 7e) had a core level shift of 3.2 eV (core level binding energy near 287.8 eV) relative to C–C; this binding energy is in the same range of C=O functional groups [45]. The presence of vacancies also affects the core level binding energy, as these vacancies create a new distribution of the electrons causing strained structures or reconstruction of the structures [72]—hence, a significant impact on the core level binding energy of the atoms.

The FWHM of C–C can relax in the range of 1.2–2.0 eV, due to fitting parameters obtained from the known compounds. The G-L function of the C 1s core level binding energy can relax between

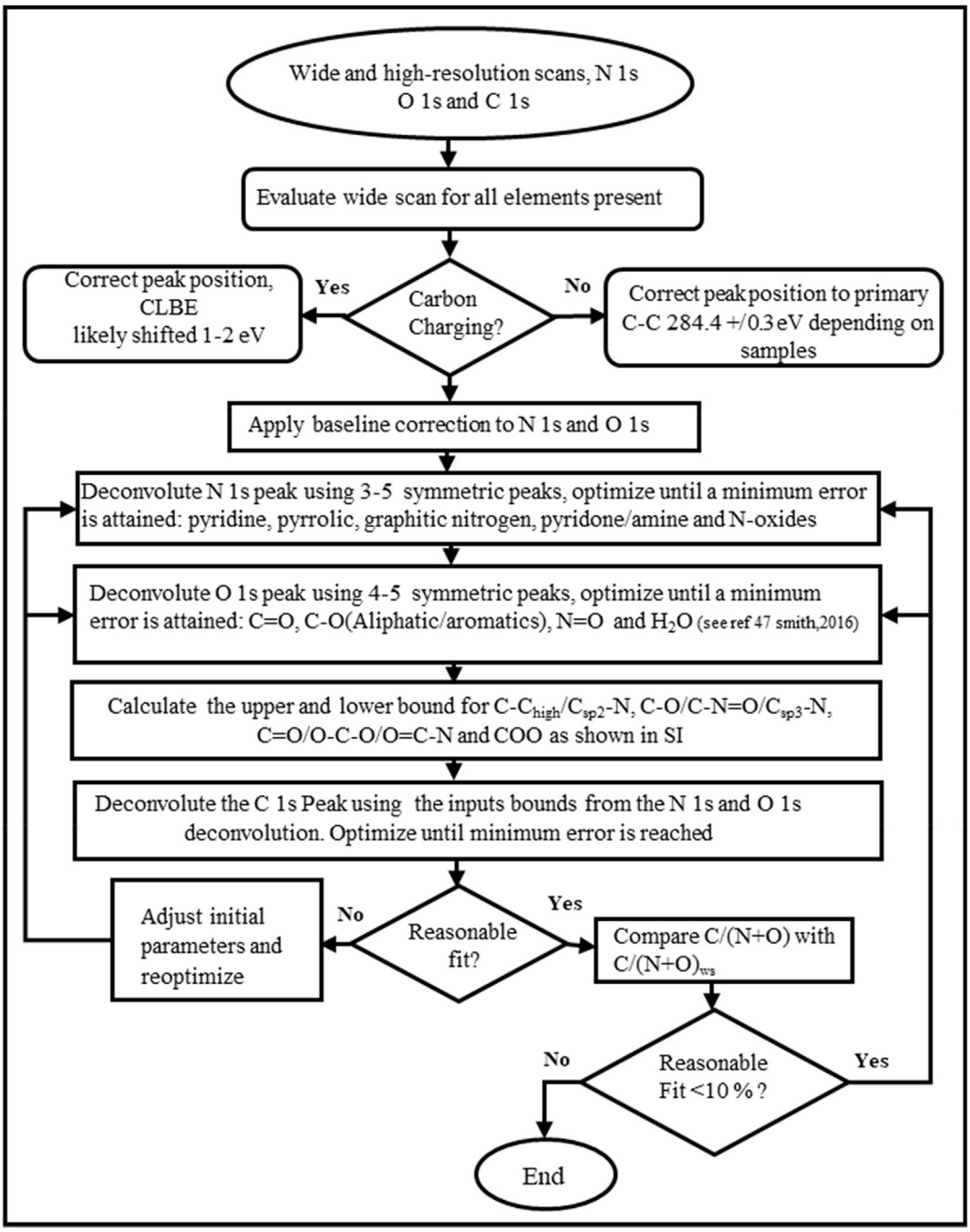

Fig. 10. Basic algorithm for the combined N 1s/O 1s/C 1s deconvolution of XPS spectra of chars and amorphous carbons. The algorithm has been modified from Smith et al. for nitrogenated carbons [45].

0 and 30%; a maximum bound of 30% (meaning 30% Lorentzian and 70% Gaussian) while a G-L of 20% was obtained for the N 1s. This indicates that the deconvolution of the XPS data of carbonaceous materials is best performed by a combination of both Gaussian and Lorentzian functions as these shapes arise due to a combination of the physics involved in the ionization process and distortions due to the measurement mechanism. It is important to mention that the peak asymmetry of the primary C–C band for chars produced at elevated temperatures is most likely a result of secondary emissions effects. This effect is linked to the increased aromatic condensation of these materials and is a well-known effect in both graphite and activated carbons. Proper consideration of the asymmetry factor of the primary C–C peak is essential for the accurate deconvolution of the C1s spectrum. This asymmetry is attributed to the excitation of conduction band electrons following a core emission. Hence, to be able to capture the effect of the secondary emission effect, the primary C–C (peak II) assigned to aromatic carbons, is allowed a variable asymmetry factor based on the empirical equation utilized in XPSpeak 4.1 with the TL value fixed at 200. To maintain consistency with both background assessment and peak shape, the asymmetric primary C–C peak near 284.4 eV is evaluated using the full empirical AGLsum lineshape with TL fixed at 200.

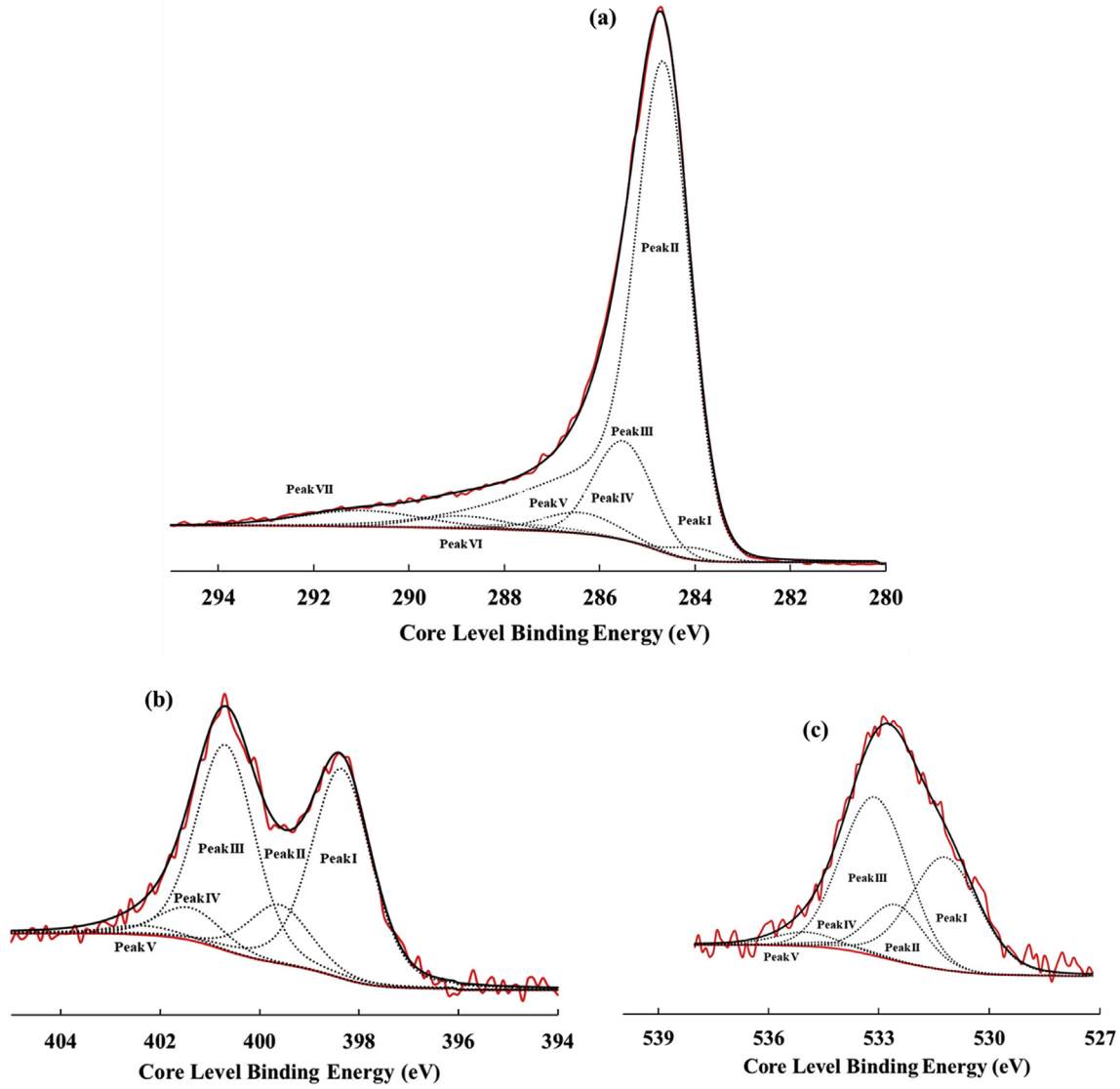

Fig. 11. Deconvolution of (a) C 1s spectra from char produced at 700 °C (where Peak I are defective carbons in five-member rings, Peak II are graphitic carbons, Peak III are carbons in more than six-member rings and C_{sp2}-N, Peak IV is C–O/C_{sp3}-N/C–N=O, Peak V is C=O/N-(C_{sp2} = O)/N–C(O)–C, Peak VI is C(O)–O/N–C(N)–N/N–C(O)–N and Peak VII is π-π*) and (b) N 1s (where Peak I is pyridinic N, Peak II is pyridone N, Peak III is pyrrolic N, Peak IV is graphitic N, and Peak V is nitrogen oxides) and (c) O 1s (where Peak I is C=O, Peak II is O–C aliphatic, Peak III is O–C aromatics N, Peak IV is Oxygen bonded to nitrogen, and Peak V is water due to the moisture content). (A colour version of this figure can be viewed online.)

Table 6
Percentage of peak composition after using a newly proposed scheme for the deconvolution of chars produced from 350 to 700 °C.

Deconvoluted Peaks		Carbonization Temperature				
		350 °C	400 °C	500 °C	600 °C	700 °C
		Peak composition				
C–C $_{low\ Defect}$	(%)	8.3	16.1	2.8	1.8	1.3
C–C $_{Primary}$	(%)	32.8	36.9	66.7	70.1	74.8
C–C $_{High}$/C_{sp2}-N	(%)	30.5	23.9	17.4	15.0	12.9
C–O/C–N=O/C_{sp3}-N	(%)	12.0	11.8	5.1	4.2	3.5
C=O/O=C–N	(%)	11.4	7.4	3.1	3.9	1.2
COO	(%)	3.9	2.6	2.1	1.9	2.5
π-π*	(%)	1.4	1.4	3.0	3.1	4.4
C/(N + O) $_{ws}$		2.8	3.6	4.8	6.4	9.0
C/(N + O)		2.9	3.4	4.7	6.4	9.2
C/(N + O)$_{error}$	(%)	−4.8	4.3	3.0	−0.2	−2.3

ws-wide scan from XPS experiment.

Table 7
Peak positions after deconvolution analysis of char produced from 350 to 700 °C.

Deconvoluted Peaks	Carbonization Temperature				
	350 °C	400 °C	500 °C	600 °C	700 °C
	Peak Center (eV)				
C–C $_{low\ Defect}$	283.3	283.4	284.0	284.0	284.0
C–C $_{Primary}$	284.3	284.5	284.5	284.6	284.7
C–C $_{High}$/C_{sp2}-N	285.3	285.1	285.2	285.5	285.5
C–O/C–N=O/C_{sp3}-N	286.1	286.2	285.9	285.9	286.4
C=O/O=C–N	287.5	287.5	286.7	286.9	287.5
COO	288.8	288.8	288.9	288.8	288.9
π-π*	291.0	291.0	291.1	291.0	291.0

Table 8
Full width half maximum (FWHM) after deconvolution analysis of char produced from 350 to 700 °C.

Deconvoluted Peaks	Carbonization Temperature				
	350 °C	400 °C	500 °C	600 °C	700 °C
	FWHM				
C–C $_{low\ Defect}$	1.8	1.8	1.2	1.2	1.2
C–C $_{Primary}$	1.5	1.4	1.4	1.4	1.3
C–C $_{High}$/C_{sp2}-N	1.6	1.8	1.7	1.8	1.4
C–O/C–N=O/C_{sp3}-N	1.9	2.0	1.8	2.2	1.8
C=O/O=C–N	1.9	1.8	2.0	1.9	2.2
COO	1.9	2.0	1.8	1.8	2.2
π-π*	2.6	2.3	3.0	3.0	3.0

3.6. Deconvolution of N-doped cellulose char using the newly proposed rules

Finally, using the established rules (summarized results in Table 5), we were able to deconvolute the XPS spectra of N-doped cellulose char. Fig. 10 shows a basic algorithm proposed to serve as a systematic approach toward deconvoluting amorphous nitrogenated carbonaceous materials like char. Fig. 11 shows the deconvoluted spectra of char that contains nitrogen, carbon and oxygen and is produced at 700 °C. The N 1s spectra has been partitioned into 5 peaks: pyridinic (Peak I) (398.4 eV), pyridone (Peak II) (399.6 eV), pyrrolic (Peak III) (400.6 eV), graphitic (Peak IV) (401.2 eV), and N-oxide (Peak V) (402.1 eV). The O 1s is deconvoluted into 5 peaks: C=O (Peak I), 531.2 eV; C–O aliphatic (Peak II), 532.5 eV; C–O aromatic (Peak III), 533.1 eV; N=O (Peak IV), 534.1 eV and H_2O (Peak V) 534.9 eV. Whereas the C 1s spectra was deconvoluted into 7 peaks: C-C_{low} (Peak I), 283.8 eV; C-$C_{primary}$ (Peak II), 284.6 eV; C-C_{high}/C_{sp2}-N (Peak III), 285.4 eV; C–O/C–N=O/C_{sp3}-N (Peak IV), 286.0 eV; C=O/O=C–N (Peak V), 286.7 eV and N–C=O (Peak VI), 288.8 eV peaks as well as a π-π* transition peak (Peak VII) located at 291 eV.

Deconvolution of the N-doped cellulose char gives an understanding of how the different structural configuration of C–C, C–N and C–O changes with the production temperature. Tables 6–8 presents the composition, peak position and the FWHM of carbon spectra at different temperatures after applying our newly proposed deconvolution strategy for nitrogenated amorphous char respectively. The increase in carbonization temperature from 350 to 700 °C has a significant effect on the structure of the resulting char. The formation of graphitic structures (C–C $_{primary}$) is lower at 350 °C and disordered and defective carbons tend to dominate around these temperatures. This can be explained from the fact that these temperatures are not sufficient to cause significant polycondensation reactions. As the temperature rises, there is a higher degree of polycondensation leading to more sp^2 carbons, which decreases the level of disorder and defects due to the formation of partially well-defined polyaromatics structures. Considering the heteroatoms in the system, it is obvious to see the reduction trend of both oxygen and nitrogen functionalities as a function of carbonization temperature. Another important factor to note is that the satellite peak (π-π*) increases as the temperature increases. This is related to the fact that more aromatic structures (more C_{sp2}) are being formed. Using the newly proposed scheme we have been able to describe the intrinsic nature of the nitrogen and oxygen distributions within the char resulting in an error of less than 5% between the total experimental C/$(N + O)_{ws}$ (where ws denotes that this is the wide scan from the XPS experiment) and the C/(N + O) ratio estimated after the deconvolution process.

Here, a systematic approach has been developed to interpret XPS spectra of nitrogenated carbons. The analysis given above demonstrates that a careful deconvolution of the binding states of amorphous carbons like char requires the consideration and evaluation of extrinsic effects, such as line broadening, as well as intrinsic effects, such as the degree of functionalization and contributions of carbon species distinct from graphite carbon in an inhomogeneous system. Our analysis gives insight into the structural configuration of nitrogenated amorphous carbons and their defects (such as vacancies and disorder), the latter of which have a high affinity to foreign atoms/molecules [74]. This analysis also helps to determine how the carbonization temperature during char creation affects the formation of non-hexagonal ring structures.

4. Conclusion

A new curve deconvolution scheme has been proposed for amorphous, nitrogen containing carbons that utilizes deconvolution of the N 1s and O 1s peak as a frontier parameter for the interpretation of the C 1s peak. The deconvolution of C 1s was achieved with the help of DFT-based calculations. These calculated results provided an insight into the C 1s core level binding energy shifts caused by different nitrogenated functional groups leading to the prediction of peak positions. With the DFT calculated results we determined that nitrogen and oxygen functionalities can overlap, such as C–O/C_{sp3}-N/C–N=O, C=O/N-(C_{sp2} = O)/N–C(O)–C as well as C(O)–O/N–C(N)–N/N–C(O)–N. Notwithstanding that, defective carbons in more than 6-membered rings (C-C_{high}) can also overlap with C_{sp2}-N. The results from the deconvolution of spectra from nitrogen containing char indicated the presence of defects in the form of non-hexagonal rings. Identification of these surface defect components allows a high-quality deconvolution of C 1s spectra. The deconvolution method proposed was based on the information available in the literature and on DFT-based calculations of primary effects of polyaromatic structures containing N and O functional groups. Secondary emission effects need to be taken into account in the deconvolution of the C1s XPS spectra. In our deconvolution scheme, the secondary effect was taken into account with an empirical equation describing the asymmetry of the primary C–C peak. New phenomenological studies of secondary effect (DFT or of other nature) are needed to inform the creation of more robust deconvolution schemes for carbons containing O and N.

Declaration of competing interest

The authors declare that they have no known competing financial interests or personal relationships that could have appeared to influence the work reported in this paper.

CRediT authorship contribution statement

Michael Ayiania: Conceptualization, Methodology, Software, Validation, Formal analysis, Investigation, Writing - original draft,

Writing - review & editing, Visualization. **Matthew Smith:** Methodology, Software, Validation, Formal analysis, Writing - review & editing. **Alyssa J.R. Hensley:** Methodology, Software, Validation, Formal analysis, Writing - review & editing. **Louis Scudiero:** Methodology, Investigation, Resources. **Jean-Sabin McEwen:** Conceptualization, Methodology, Resources, Data curation, Writing - review & editing, Supervision, Project administration, Funding acquisition. **Manuel Garcia-Perez:** Conceptualization, Resources, Writing - review & editing, Supervision, Project administration, Funding acquisition.

Acknowledgements

This work was supported by the National Science Foundation under Contract No. CBET-1703052. The authors thank Aidan Garcia for their helpful comments and discussions. We would like to thank the Murdock Charitable trust fund for its financial support in upgrading our existing XPS instrument. Dr. Garcia-Perez would like to thank the Washington State Applied Bioenergy program (Appendix A), the Sun Grant Initiative (Federal USDA/NIFA award: 2014-38502-22598) and USDA/NIFA through Hatch Project # WNP0002 for the financial support provided. This research used resources from the Center for Institutional Research Computing at Washington State University. PNNL is a multiprogram national laboratory operated for the US DOE by Battelle.

Appendix A. Supplementary data

Supplementary data to this article can be found online at https://doi.org/10.1016/j.carbon.2020.02.065.

References

[1] I. Hilber, F. Blum, J. Leifeld, H.-P. Schmidt, T.D. Bucheli, Quantitative determination of PAHs in biochar: a prerequisite to ensure its quality and safe application, J. Agric. Food Chem. 60 (2012) 3042–3050.
[2] H. Estrade-Szwarckopf, XPS photoemission in carbonaceous materials: a "defect" peak beside the graphitic asymmetric peak, Carbon 42 (2004) 1713–1721.
[3] R. Blume, D. Rosenthal, J.P. Tessonnier, H. Li, A. Knop-Gericke, R. Schlögl, Characterizing graphitic carbon with X-ray photoelectron spectroscopy: a step-by-step approach, ChemCatChem 7 (2015) 2871–2881.
[4] Y. Yao, B. Gao, J. Chen, L. Yang, Engineered biochar reclaiming phosphate from aqueous solutions: mechanisms and potential application as a slow-release fertilizer, Environ. Sci. Technol. 47 (2013) 8700–8708.
[5] Y. Yao, B. Gao, J. Chen, M. Zhang, M. Inyang, Y. Li, et al., Engineered carbon (biochar) prepared by direct pyrolysis of Mg-accumulated tomato tissues: characterization and phosphate removal potential, Bioresour. Technol. 138 (2013) 8–13.
[6] Y. Yao, B. Gao, M. Zhang, M. Inyang, A.R. Zimmerman, Effect of biochar amendment on sorption and leaching of nitrate, ammonium, and phosphate in a sandy soil, Chemosphere 89 (2012) 1467–1471.
[7] M. Zhang, B. Gao, Y. Yao, Y. Xue, M. Inyang, Synthesis of porous MgO-biochar nanocomposites for removal of phosphate and nitrate from aqueous solutions, Chem. Eng. J. 210 (2012) 26–32.
[8] M. Zhang, B. Gao, S. Varnoosfaderani, A. Hebard, Y. Yao, M. Inyang, Preparation and characterization of a novel magnetic biochar for arsenic removal, Bioresour. Technol. 130 (2013) 457–462.
[9] X. Wang, X. Li, L. Zhang, Y. Yoon, P.K. Weber, H. Wang, et al., N-doping of graphene through electrothermal reactions with ammonia, Science 324 (2009) 768–771.
[10] D. Yu, E. Nagelli, F. Du, L. Dai, Metal-free carbon nanomaterials become more active than metal catalysts and last longer, J. Phys. Chem. Lett. 1 (2010) 2165–2173.
[11] L. Zhang, J. Zhang, D.P. Wilkinson, H. Wang, Progress in preparation of non-noble electrocatalysts for PEM fuel cell reactions, J. Power Sources 156 (2006) 171–182.
[12] M. Lefèvre, E. Proietti, F. Jaouen, J.-P. Dodelet, Iron-based catalysts with improved oxygen reduction activity in polymer electrolyte fuel cells, Science 324 (2009) 71–74.
[13] G. Wu, K.L. More, C.M. Johnston, P. Zelenay, High-performance electrocatalysts for oxygen reduction derived from polyaniline, iron, and cobalt, Science 332 (2011) 443–447.
[14] E. Proietti, F. Jaouen, M. Lefèvre, N. Larouche, J. Tian, J. Herranz, et al., Iron-based cathode catalyst with enhanced power density in polymer electrolyte membrane fuel cells, Nat. Commun. 2 (2011) 416.
[15] D.H. Lee, W.J. Lee, W.J. Lee, S.O. Kim, Y.-H. Kim, Theory, synthesis, and oxygen reduction catalysis of Fe-porphyrin-like carbon nanotube, Phys. Rev. Lett. 106 (2011), 175502.
[16] D. Deng, X. Pan, L. Yu, Y. Cui, Y. Jiang, J. Qi, et al., Toward N-doped graphene via solvothermal synthesis, Chem. Mater. 23 (2011) 1188–1193.
[17] R.I. Jafri, N. Rajalakshmi, S. Ramaprabhu, Nitrogen doped graphene nanoplatelets as catalyst support for oxygen reduction reaction in proton exchange membrane fuel cell, J. Mater. Chem. 20 (2010) 7114–7117.
[18] Y.-H. Lu, M. Zhou, C. Zhang, Y.-P. Feng, Metal-embedded graphene: a possible catalyst with high activity, J. Phys. Chem. C 113 (2009) 20156–20160.
[19] D. Geng, Y. Chen, Y. Chen, Y. Li, R. Li, X. Sun, et al., High oxygen-reduction activity and durability of nitrogen-doped graphene, Energy Environ. Sci. 4 (2011) 760–764.
[20] Y. Cheng, S. Zhao, H. Li, S. He, J.-P. Veder, B. Johannessen, et al., Unsaturated edge-anchored Ni single atoms on porous microwave exfoliated graphene oxide for electrochemical CO_2, Appl. Catal. B Environ. 243 (2019) 294–303.
[21] H. Chen, F. Sun, J. Wang, W. Li, W. Qiao, L. Ling, et al., Nitrogen doping effects on the physical and chemical properties of mesoporous carbons, J. Phys. Chem. C 117 (2013) 8318–8328.
[22] F. Adib, A. Bagreev, T.J. Bandosz, Adsorption/oxidation of hydrogen sulfide on nitrogen-containing activated carbons, Langmuir 16 (2000) 1980–1986.
[23] M. Nandi, K. Okada, A. Dutta, A. Bhaumik, J. Maruyama, D. Derks, et al., Unprecedented CO_2 uptake over highly porous N-doped activated carbon monoliths prepared by physical activation, Chem. Commun. 48 (2012) 10283–10285.
[24] Y. Shao, X. Wang, M. Engelhard, C. Wang, S. Dai, J. Liu, et al., Nitrogen-doped mesoporous carbon for energy storage in vanadium redox flow batteries, J. Power Sources 195 (2010) 4375–4379.
[25] Y. Li, J. Wang, X. Li, J. Liu, D. Geng, J. Yang, et al., Nitrogen-doped carbon nanotubes as cathode for lithium–air batteries, Electrochem. Commun. 13 (2011) 668–672.
[26] L.L. Zhang, X. Zhao, H. Ji, M.D. Stoller, L. Lai, S. Murali, et al., Nitrogen doping of graphene and its effect on quantum capacitance, and a new insight on the enhanced capacitance of N-doped carbon, Energy Environ. Sci. 5 (2012) 9618–9625.
[27] P. Chen, T.Y. Xiao, Y.H. Qian, S.S. Li, S.H. Yu, A Nitrogen-doped graphene/carbon nanotube nanocomposite with synergistically enhanced electrochemical activity, Adv. Mater. 25 (2013) 3192–3196.
[28] V. Sahu, S. Grover, B. Tulachan, M. Sharma, G. Srivastava, M. Roy, et al., Heavily nitrogen doped, graphene supercapacitor from silk cocoon, Electrochim. Acta 160 (2015) 244–253.
[29] E. Frackowiak, F. Beguin, Electrochemical storage of energy in carbon nanotubes and nanostructured carbons, Carbon 40 (2002) 1775–1787.
[30] A. Alfarra, E. Frackowiak, F. Béguin, Mechanism of lithium electrosorption by activated carbons, Electrochim. Acta 47 (2002) 1545–1553.
[31] Z. Wang, L. Qie, L. Yuan, W. Zhang, X. Hu, Y. Huang, Functionalized N-doped interconnected carbon nanofibers as an anode material for sodium-ion storage with excellent performance, Carbon 55 (2013) 328–334.
[32] L. Lai, J.R. Potts, D. Zhan, L. Wang, C.K. Poh, C. Tang, et al., Exploration of the active center structure of nitrogen-doped graphene-based catalysts for oxygen reduction reaction, Energy Environ. Sci. 5 (2012) 7936–7942.
[33] Z.-H. Sheng, L. Shao, J.-J. Chen, W.-J. Bao, F.-B. Wang, X.-H. Xia, Catalyst-free synthesis of nitrogen-doped graphene via thermal annealing graphite oxide with melamine and its excellent electrocatalysis, ACS Nano 5 (2011) 4350–4358.
[34] J.-Y. Liu, H.-Y. Chang, Q.D. Truong, Y.-C. Ling, Synthesis of nitrogen-doped graphene by pyrolysis of ionic-liquid-functionalized graphene, J. Mater. Chem. 1 (2013) 1713–1716.
[35] U. Byambasuren, Y. Jeon, D. Altansukh, Y. Ji, Y.-G. Shul, One-step synthesis of dual-transition metal substitution on ionic liquid based N-doped mesoporous carbon for oxygen reduction reaction, Carbon lett 17 (2016) 53–64.
[36] C.L. Mangun, K.R. Benak, J. Economy, K.L. Foster, Surface chemistry, pore sizes and adsorption properties of activated carbon fibers and precursors treated with ammonia, Carbon 39 (2001) 1809–1820.
[37] W. Chen, H. Yang, Y. Chen, X. Chen, Y. Fang, H. Chen, Biomass pyrolysis for nitrogen-containing liquid chemicals and nitrogen-doped carbon materials, J. Anal. Appl. Pyrolysis 120 (2016) 186–193.
[38] W. Luo, B. Wang, C.G. Heron, M.J. Allen, J. Morre, C.S. Maier, et al., Pyrolysis of cellulose under ammonia leads to nitrogen-doped nanoporous carbon generated through methane formation, Nano Lett. 14 (2014) 2225–2229.
[39] J. Lahaye, G. Nanse, A. Bagreev, V. Strelko, Porous structure and surface chemistry of nitrogen containing carbons from polymers, Carbon 37 (1999) 585–590.
[40] Y. El-Sayed, T. Bandosz, An IGC and TA study of acetaldehyde adsorption on activated carbons, Stud. Surf. Sci. Catal. (2002) 247–254.
[41] K. Ghosh, M. Kumar, T. Maruyama, Y. Ando, Tailoring the field emission property of nitrogen-doped carbon nanotubes by controlling the graphitic/pyridinic substitution, Carbon 48 (2010) 191–200.
[42] E. Ibrahim, V.O. Khavrus, A. Leonhardt, S. Hampel, S. Oswald, M.H. Rümmeli, et al., Synthesis, characterization, and electrical properties of nitrogen-doped single-walled carbon nanotubes with different nitrogen content, Diam. Relat. Mater. 19 (2010) 1199–1206.
[43] W. Ouyang, D. Zeng, X. Yu, F. Xie, W. Zhang, J. Chen, et al., Exploring the active sites of nitrogen-doped graphene as catalysts for the oxygen reduction

reaction, Int. J. Hydrogen Energy 39 (2014) 15996–16005.
[44] Q. Liu, Y. Zhou, S. Chen, Z. Wang, H. Hou, F. Zhao, Cellulose-derived nitrogen and phosphorus dual-doped carbon as high performance oxygen reduction catalyst in microbial fuel cell, J. Power Sources 273 (2015) 1189–1193.
[45] M. Smith, L. Scudiero, J. Espinal, J.-S. McEwen, M. Garcia-Perez, Improving the deconvolution and interpretation of XPS spectra from chars by ab initio calculations, Carbon 110 (2016) 155–171.
[46] J.P. Tessonnier, M. Becker, W. Xia, F. Girgsdies, R. Blume, L. Yao, et al., Spinel type cobalt–manganese based mixed oxide as sacrificial catalyst for the high yield production of homogeneous carbon nanotubes, ChemCatChem 2 (2010) 1559–1561.
[47] S.A. Steiner III, T.F. Baumann, B.C. Bayer, R. Blume, M.A. Worsley, W.J. MoberlyChan, et al., Nanoscale zirconia as a nonmetallic catalyst for graphitization of carbon and growth of single-and multiwall carbon nanotubes, J. Am. Chem. Soc. 131 (2009) 12144–12154.
[48] R.S. Weatherup, H. Amara, R. Blume, B. Dlubak, B.C. Bayer, M. Diarra, et al., Interdependency of subsurface carbon distribution and graphene–catalyst interaction, J. Am. Chem. Soc. 136 (2014) 13698–13708.
[49] P. Wu, Y. Qian, P. Du, H. Zhang, C. Cai, Facile synthesis of nitrogen-doped graphene for measuring the releasing process of hydrogen peroxide from living cells, J. Mater. Chem. 22 (2012) 6402–6412.
[50] N. Hellgren, R.T. Haasch, S. Schmidt, L. Hultman, I. Petrov, Interpretation of X-ray photoelectron spectra of carbon-nitride thin films: new insights from in situ XPS, Carbon 108 (2016) 242–252.
[51] A. Proctor, P.M. Sherwood, X-ray photoelectron spectroscopic studies of carbon fibre surfaces—II: the effect of electrochemical treatment, Carbon 21 (1983) 53–59.
[52] J. Pels, F. Kapteijn, J. Moulijn, Q. Zhu, K. Thomas, Evolution of nitrogen functionalities in carbonaceous materials during pyrolysis, Carbon 33 (1995) 1641–1653.
[53] A.L.M. Reddy, A. Srivastava, S.R. Gowda, H. Gullapalli, M. Dubey, P.M. Ajayan, Synthesis of nitrogen-doped graphene films for lithium battery application, ACS Nano 4 (2010) 6337–6342.
[54] M.W. Smith, I. Dallmeyer, T.J. Johnson, C.S. Brauer, J.-S. McEwen, J.F. Espinal, et al., Structural analysis of char by Raman spectroscopy: improving band assignments through computational calculations from first principles, Carbon 100 (2016) 678–692.
[55] Z. Wang, A.G. McDonald, R.J. Westerhof, S.R. Kersten, C.M. Cuba-Torres, S. Ha, et al., Effect of cellulose crystallinity on the formation of a liquid intermediate and on product distribution during pyrolysis, J. Anal. Appl. Pyrolysis 100 (2013) 56–66.
[56] A.D. Becke III, Density-functional thermochemistry the role of exact exchange, J. Chem. Phys. 98 (1993) 5648–5652.
[57] Y.Y. Yamada, Hajime, Kazumasa Murota, Masashi Nakamura, Toshiaki Sodesawa, Satoshi Sato, Analysis of heat-treated graphite oxide by X-ray photoelectron spectroscopy, Carbon 48 (2013) 8171–8198.
[58] Y. Yamada, J. Kim, S. Matsuo, S. Sato, Nitrogen-containing graphene analyzed by X-ray photoelectron spectroscopy, Carbon 70 (2014) 59–74.
[59] G. Kresse, J. Hafner, Ab initio molecular dynamics for liquid metals, Phys. Rev. B 47 (1993) 558.
[60] G. Kresse, J. Furthmüller, Efficiency of ab-initio total energy calculations for metals and semiconductors using a plane-wave basis set, Comput. Mater. Sci. 6 (1996) 15–50.
[61] G. Kresse, J. Furthmüller, Efficient iterative schemes for ab initio total-energy calculations using a plane-wave basis set, Phys. Rev. B 54 (1996) 11169.
[62] M.W. Smith, B. Pecha, G. Helms, L. Scudiero, M. Garcia-Perez, Chemical and morphological evaluation of chars produced from primary biomass constituents: cellulose, xylan, and lignin, Biomass Bioenergy 104 (2017) 17–35.
[63] H. Kawamoto, M. Murayama, S. Saka, Pyrolysis behavior of levoglucosan as an intermediate in cellulose pyrolysis: polymerization into polysaccharide as a key reaction to carbonized product formation, J. Wood Sci. 49 (2003) 469–473.
[64] S.-S. Liaw, S. Zhou, H. Wu, M. Garcia-Perez, Effect of pretreatment temperature on the yield and properties of bio-oils obtained from the auger pyrolysis of Douglas fir wood, Fuel 103 (2013) 672–682.
[65] Z. Wang, B. Pecha, R.J. Westerhof, S.R. Kersten, C.-Z. Li, A.G. McDonald, et al., Effect of cellulose crystallinity on solid/liquid phase reactions responsible for the formation of carbonaceous residues during pyrolysis, Ind. Eng. Chem. Res. 53 (2014) 2940–2955.
[66] H.P. Boehm, Surface oxides on carbon and their analysis: a critical assessment, Carbon 40 (2002) 145–149.
[67] J.A. Menéndez, B. Xia, J. Phillips, L.R. Radovic, On the modification and characterization of chemical surface properties of activated carbon: microcalorimetric, electrochemical, and thermal desorption probes, Langmuir 13 (1997) 3414–3421.
[68] Y. Sui, B. Zhu, H. Zhang, H. Shu, Z. Chen, Y. Zhang, et al., Temperature-dependent nitrogen configuration of N-doped graphene by chemical vapor deposition, Carbon 81 (2015) 814–820.
[69] S. Kabir, K. Artyushkova, A. Serov, B. Kiefer, P. Atanassov, Binding energy shifts for nitrogen-containing graphene-based electrocatalysts–experiments and DFT calculations, Surf. Interface Anal. 48 (2016) 293–300.
[70] K. Artyushkova, B. Kiefer, B. Halevi, A. Knop-Gericke, R. Schlogl, P. Atanassov, Density functional theory calculations of XPS binding energy shift for nitrogen-containing graphene-like structures, Chem. Commun. 49 (2013) 2539–2541.
[71] CASAXPS, Peak Fitting in XPS, 2006.
[72] M. Ayiania, A.J. Hensley, K. Groden, M. Garcia-Perez, J.-S. McEwen, Thermodynamic stability of nitrogen functionalities and defects in graphene and graphene nanoribbons from first principles, Carbon 152 (2019) 715–726.
[73] M.W. Smith, G. Helms, J.-S. McEwen, M. Garcia-Perez, Effect of pyrolysis temperature on aromatic cluster size of cellulose char by quantitative multi cross-polarization 13 C NMR with long range dipolar dephasing, Carbon 116 (2017) 210–222.
[74] A. Krasheninnikov, R. Nieminen, Attractive interaction between transition-metal atom impurities and vacancies in graphene: a first-principles study, Theor. Chem. Acc. 129 (2011) 625–630.